Transport Dynamics of Water Molecules Confined between Lipid Membranes

Minho Lee[1, 2], Euihyun Lee[3], Ji-Hyun Kim[1, 2], Hyonseok Hwang[6], Minhaeng Cho[4, 5]*, and Jaeyoung Sung[1, 2]*

[1] Creative Research Initiative Center for Chemical Dynamics in Living Cells, Chung-Ang University, Seoul 06974, Republic of Korea

[2] Department of Chemistry, Chung-Ang University, Seoul 06974, Republic of Korea

[3] Department of Chemistry, The University of Texas at Austin, TX 78757, USA

[4] Center for Molecular Spectroscopy and Dynamics, Institute for Basic Science (IBS), Seoul 02841, Republic of Korea

[5] Department of Chemistry, Korea University, Seoul 02841, Republic of Korea

[6] Department of Chemistry, Institute for Molecular Science and Fusion Technology, Kangwon National University, Chuncheon, Gangwon-do 24341, Republic of Korea

*Correspondence and requests for materials should be addressed to J.S. (email: jaeyoung@cau.ac.kr) and M.C. (email: mcho@korea.ac.kr).

ABSTRACT

Water molecules confined between biological membranes exhibit a distinctive non-Gaussian displacement distribution, far different from bulk water. Here, we introduce a new transport equation for water molecules in the intermembrane space, quantitatively explaining molecular dynamics simulation results. We find that the unique transport dynamics of water molecules stems from the lateral diffusion coefficient fluctuation caused by their longitudinal motion in the direction perpendicular to the membranes. We also identify an interfacial region where water possesses distinct physical properties, unaffected by changes in the intermembrane separation.

TOC GRAPHICS
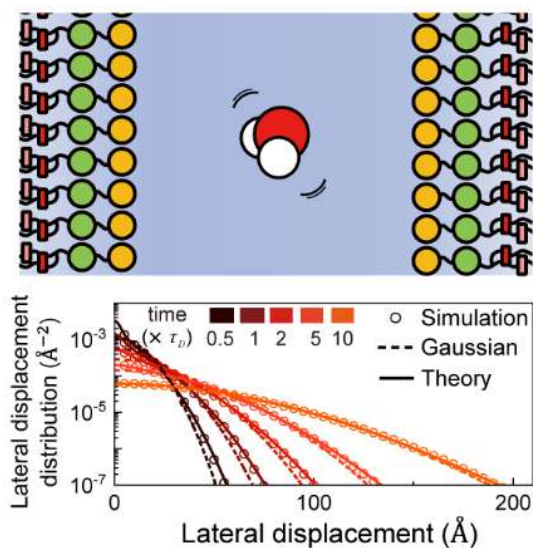
KEYWORDS

Nanochannel, Lipid bilayers, Heterogeneity, Complex fluids, Transport equation

Water confined in biological nanospaces, such as the inter-membrane regions of mitochondria, synaptic clefts, and endoplasmic reticula, is a crucial element for cell function[1–3]. Extensive research has investigated the structure and dynamics of water molecules in the vicinity of phosphatidylcholine (PC) bilayers, a major component of biological membranes. These works employed various methods including IR pump-probe spectroscopy[4–6], heterodyne-detected vibration sum frequency generation (HD-VSFG)[7,8], nuclear magnetic resonance (NMR)[9], microfluidics[10–12], and molecular dynamics (MD) simulation[13–21]. It is now established that the motility of nanoconfined water increases with its distance from the membrane center, with which the major functional groups of PC phospholipids interacting with water molecules change[4,9,14,17,18]. Moreover, it has been observed that dynamic motility fluctuations lead to Fickian-yet-non-Gaussian diffusion in complex fluids[22]. Despite these studies, however, a quantitative understanding of the time-dependent displacement distribution of nanoconfined water molecules has not yet been achieved.

To address this issue, we introduce a transport equation describing the thermal motion of molecules confined between two planar surfaces. Using MD simulations, we investigate the time-dependent displacement distribution of water molecules nanoconfined between two lipid membranes composed of 1,2-dimyristoyl-sn-glycero-3-phosphocholine (DMPC) lipids. The solution derived from our transport equation provides a quantitative explanation of the MD simulation results for the mean square displacement, the non-Gaussian parameter, and the displacement distribution. Our analysis shows that nanoconfined water exhibits a super-Gaussian lateral displacement distribution originating from dynamic fluctuations of the lateral diffusion coefficient due to its coupling to water motion in the longitudinal direction. The time-dependent deviation of this lateral displacement distribution from Gaussian is found to be strongly influenced

by the intermembrane separation. We also identify an interfacial region where water molecules have structure and dynamics that are distinct from bulk water and robust with respect to changes in intermembrane separation.

The essential assumption underlying our transport equation is that the most important variable that affects the lateral thermal motion of an interfacial water molecule is the distance, z, between the water molecule and the center of the membrane. This is a legitimate assumption because the microscopic environment interacting with a water molecule, including the functional groups of lipid molecules and hydrogen bond network, drastically changes with z[9,17,18]. Under this assumption, we obtain the following transport equation governing transport dynamics of interfacial water, starting from a general model of thermal motion coupled to environmental variables[23]:

$$\hat{\dot{p}}(\mathbf{r}_{\parallel},z,s) = \hat{\mathcal{D}}_{\parallel}(z,s)\nabla_{\parallel}^{2}\hat{p}(\mathbf{r}_{\parallel},z,s) + L(z)\hat{p}(\mathbf{r}_{\parallel},z,s),\qquad(1)$$

where $\hat{p}(\mathbf{r}_{\parallel},z,s)$ denotes the Laplace transform of the joint probability density, $p(\mathbf{r}_{\parallel},z,t)$, that a water molecule is located at lateral position $\mathbf{r}_{\parallel}$ $(=(x,y))$ and the distance between the water molecule and the center of the membrane is z at time t. $\hat{f}(s)$ and $\hat{\dot{f}}(s)$ denote the Laplace transform of $f(t)$ and $\partial_{t}f(t)$, i.e., $\hat{f}(s) = \int_{0}^{\infty}dt e^{-st}f(t)$ and $\hat{\dot{f}}(s) = \int_{0}^{\infty}dt e^{-st}\partial_{t}f(t)$. $\nabla_{\parallel}^{2}$ denotes the Laplacian in the two-dimensional space parallel to the lipid membrane. In eq 1, $\hat{\mathcal{D}}_{\parallel}(z,s)$ represents the lateral diffusion kernel dependent on z. Its small-s limit, $\hat{\mathcal{D}}_{\parallel}(z,0)$, serves as the lateral diffusion coefficient, $D_{\parallel}(z)$, of water molecules separated by z from the center of the membrane. In eq 1, $L(z)$ denotes a mathematical operator describing the transport dynamics of the water molecules in a direction perpendicular to the membrane surface.

We then investigate the mean square displacement (MSD), $\Delta_2(t)$, and non-Gaussian parameters (NGP), $\alpha_2(t)\left[\equiv \Delta_4(t)/(2\Delta_2(t)^2)-1\right]$, of the lateral displacement distribution of the water molecules. Here, $\Delta_2(t)$ and $\Delta_4(t)$ denote the second and fourth moments of the time-dependent distribution of the water displacement, $\Delta\mathbf{r}_\parallel(t)\left[\equiv \mathbf{r}_\parallel(t)-\mathbf{r}_\parallel(0)\right]$, in the lateral direction. The NGP vanishes when the displacement distribution is Gaussian[24,25]. From eq 1, analytic expressions of the $\Delta_2(t)$ and $\Delta_4(t)$ can be obtained as

$$\hat{\Delta}_2(s) = \frac{4}{s^2}\langle \hat{\mathcal{D}}_\parallel(s)\rangle, \tag{2a}$$

$$\hat{\Delta}_4(s) = 4s\hat{\Delta}_2(s)^2\left[1+s\hat{C}_{\mathcal{D}}(s)\right]. \tag{2b}$$

In eq 2a, $\langle \mathcal{D}_\parallel(t)\rangle$ denotes the mean diffusion kernel of water molecules. $\langle Q\rangle$ designates the average of quantity $Q(z)$ over the equilibrium distribution, $P_{eq}(z)$, of z. $\langle \mathcal{D}_\parallel(t)\rangle$ is the same as the lateral velocity autocorrelation function (VAF) of water molecules divided by 2^{23}. In eq 2b, $C_{\mathcal{D}}(t)$ denotes the lateral diffusion kernel correlation (DKC) defined by

$$\hat{C}_{\mathcal{D}}(s) = \int_0^\ell dz \int_0^\ell dz_0 \frac{\delta\hat{\mathcal{D}}_\parallel(z,s)}{\langle \hat{\mathcal{D}}_\parallel(s)\rangle}\hat{G}(z,s\,|\,z_0)\frac{\delta\hat{\mathcal{D}}_\parallel(z_0,s)}{\langle \hat{\mathcal{D}}_\parallel(s)\rangle}P_{eq}(z_0), \tag{3}$$

where 0 and ℓ denote the center positions of the two membranes confining water molecules (see Figure 1). In eq 3, $\delta\hat{\mathcal{D}}_\parallel(z,s)$ and $G(z,t\,|\,z_0)$ denote, respectively, $\hat{\mathcal{D}}_\parallel(z,s)-\langle \hat{\mathcal{D}}_\parallel(s)\rangle$ and the Green's function, or the conditional probability that a water molecule initially located at z_0 is found at z at time t, defined by $\partial_t G(z,t\,|\,z_0)=L(z)G(z,t\,|\,z_0)$ with the initial condition, $G(z,0\,|\,z_0)=\delta(z-z_0)$. Equation 2 enables us to extract the time profile of the DKC from the MSD

and the NGP or the first two nonvanishing moments of the displacement distribution (see Figure S3a in Supporting Information).

At the onset of Fickian diffusion, the NGP reaches its maximum value (Figure 2). Beyond this NGP peak time, the MSD of water molecules linearly increases with time, which results because the VAF or $\langle \mathcal{D}_\parallel(t) \rangle$ is negligibly small after the NGP peak time, i.e., $\Delta_2(t)$ $= 4 \int_0^t d\tau (t-\tau) \langle \mathcal{D}_\parallel(\tau) \rangle \cong 4t \int_0^\infty \langle \mathcal{D}_\parallel(\tau) \rangle$. At time scales longer than the NGP peak time, $L(z)$ in eq 1 can be approximated by the following Smoluchowski operator, i.e., $L(z)$ $\cong L_{\mathrm{SM}}(z) = \partial_z [D_\perp(z)(\partial_z + \partial_z \beta U(z))]$. Here, $D_\perp(z)$ and $\beta U(z)$, respectively, denote the z-dependent diffusion coefficient associated with the thermal motion of water molecules in the direction perpendicular to the membrane and the thermal energy-scaled potential of mean force with $\beta = 1/k_B T$. k_B and T denote the Boltzmann constant and temperature, respectively. After the onset of the Fickian diffusion, the MSD and NGP of the lateral diffusion of water molecules assume the following analytic forms:

$$\Delta_2(t) \cong 4 \langle D_\parallel \rangle t, \tag{4a}$$

$$\alpha_2(t) \cong \frac{2\eta_D^2}{t^2} \int_0^t dt' (t-t') \phi_D(t'). \tag{4b}$$

In eq 4, $\langle D_\parallel \rangle$ and $\eta_D^2 \left[= \langle \delta D_\parallel^2 \rangle / \langle D_\parallel \rangle^2 \right]$ denote, respectively, the mean diffusion coefficient defined by $\langle D_\parallel \rangle = \int_0^\infty \langle \mathcal{D}_\parallel(\tau) \rangle$ and the relative variance of the z-dependent lateral diffusion coefficient, with δf denoting the deviation of a quantity f from its mean, i.e., $\delta f(z) = f(z) - \langle f \rangle$. $\phi_D(t)$ denotes the normalized time-correlation function (TCF) of the lateral diffusion coefficient fluctuation, i.e.,

$$\phi_D(t) = \frac{\langle \delta D_\parallel(t) \delta D_\parallel(0) \rangle}{\langle \delta D_\parallel^2 \rangle} = \langle \delta D_\parallel^2 \rangle^{-1} \int_0^\ell dz \int_0^\ell dz_0 \delta D_\parallel(z) G_{SM}(z,t \,|\, z_0) \delta D_\parallel(z_0) P_{eq}(z_0), \quad (5)$$

where $G_{SM}(z,t \,|\, z_0)$ designates Green's function of Smoluchowski equation governing the thermal motion of water molecules in the direction perpendicular to the membranes, i.e., $\partial_t G_{SM}(z,t \,|\, z_0) = L_{SM}(z) G_{SM}(z,t \,|\, z_0)$, with the initial condition, $G_{SM}(z,0 \,|\, z_0) = \delta(z - z_0)$.

Equations 4b and 5 indicate that, for nanoconfined water molecules, the non-Gaussian diffusion in the lateral direction originates from fluctuation of the lateral diffusion coefficient coupled to water motion in the longitudinal direction. We note here that the DKC defined in eq 3 reduces to $\eta_D^2 \phi_D(t)$ at long times where the MSD linearly increases with time; the long-time profile of $C_D(t)$ extracted from the MSD and NGP time profiles of our MD simulation results is in quantitative agreement with our theoretical result for $\eta_D^2 \phi_D(t)$ calculated using eq 5. This agreement between simulation and theory supports the validity of our assumption underlying eq 1 that the dynamic fluctuation in the lateral diffusion coefficient of water molecules primarily originates from its coupling to the thermal motion of water molecules in the longitudinal direction.

We also performed MD simulation study on the thermal motion of water molecules in the intermembrane space, for a system of SPC/E water molecules confined between two lipid bilayers, each composed of 128 DMPC molecules, systematically changing the ratio of the number of water molecules to the number of lipid molecules and the distance ℓ between the two membrane centers (Figure 1). We employed the AMBER lipid 14 force field for simulation of the lipid molecules[26] and imposed periodic boundary conditions on the system. We also investigated the transport dynamics of a pure, bulk water system, using the MD simulation of 5000 SPC/E water molecules, and compared it to the transport dynamics of the nanoconfined water molecules. Our MD

simulation was conducted for a system at a temperature of 318 K in the *NVT* ensemble. Additional

information about the simulations can be found in the Supporting Information.
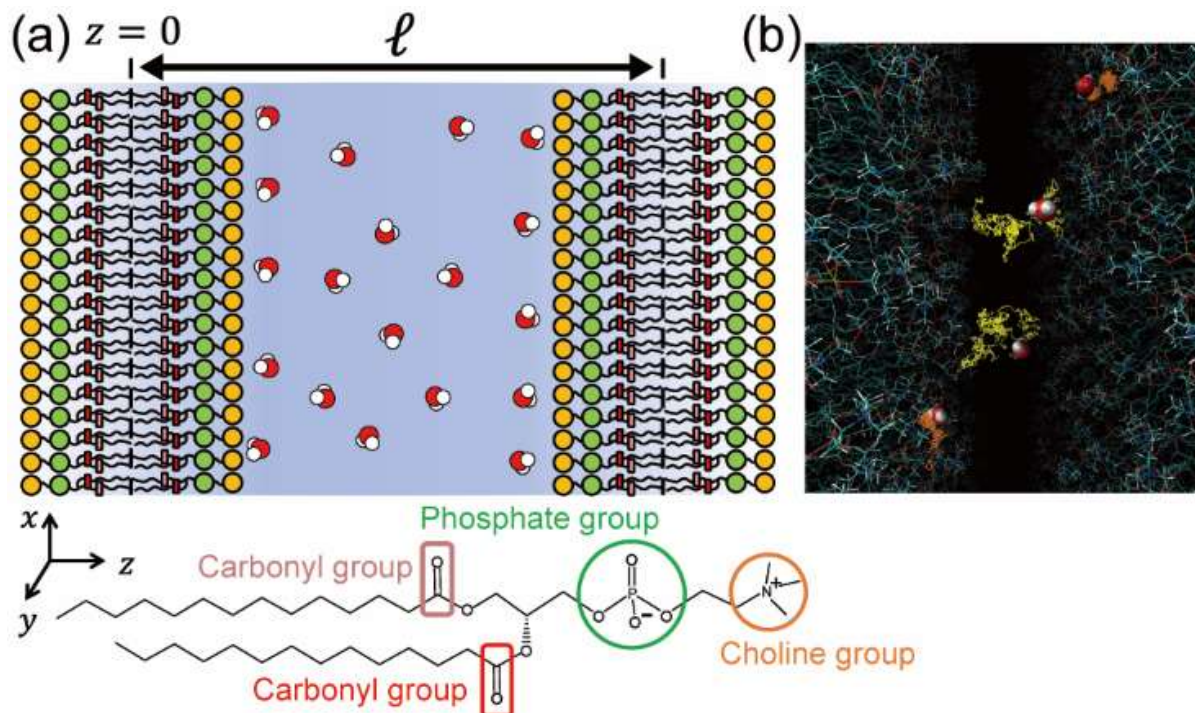

Figure 1. (a) Schematic representation of our MD simulation system: water molecules confined

between two DMPC lipid bilayers. The simulation was performed for the system with three

different intermembrane separations, i.e., ℓ = 53.2 Å, 61.8 Å, and 80.6 Å. (b) Representative

trajectories of water molecules undergoing thermal motion between the lipid bilayers for 50 ps:

(yellow lines) the trajectories of water molecules freely moving near the center of the

intermembrane space; (orange lines) trajectories of water molecules strongly interacting with the

lipid head groups of DMPC.

From the MD simulation trajectories of water molecules, we obtained the MSD and NGP of the

lateral water displacement for each system (Figure 2). The time profile of the MSD obtained from

the MD simulation exhibits a dynamic transition behavior that is dependent on the separation between the two lipid membranes (Figure 2a). The time profile of the MSD shows the transition from an initial ballistic motion ($\Delta_2(t) \sim t^2$) to terminal Fickian diffusion ($\Delta_2(t) \sim t^1$), with intermediate subdiffusion ($\Delta_2(t) \sim t^\alpha$ with $0 < \alpha < 1$). The short-time ballistic behavior of the MSD shows little variation with changes in ℓ and quadratically increases with time, i.e., $\Delta_2(t) = 2k_B T t^2 / M$ [23]. Here, M denotes the mass of a water molecule. However, the intermediate subdiffusive regime becomes more pronounced, and the value of long-time lateral diffusion coefficient gets smaller as the separation, ℓ, between lipid bilayers decreases. These findings align with previous studies[10,12,16,21]. The time profiles of the MSD could be quantitatively explained by using the analytic formula for the MSD of a bead in a Gaussian polymer (see Figure 2a), which is decomposable into an unbound-mode and multiple bound-mode terms[23]. For bulk water at room temperature, the bound-mode terms, which cause the intermediate subdiffusion, are negligible. However, for intermembrane water, the contribution from bound-modes increases as the separation, ℓ, between the membranes decreases. This indicates that the bound mode terms result from interfacial water molecules, which are transiently trapped by lipid membranes.
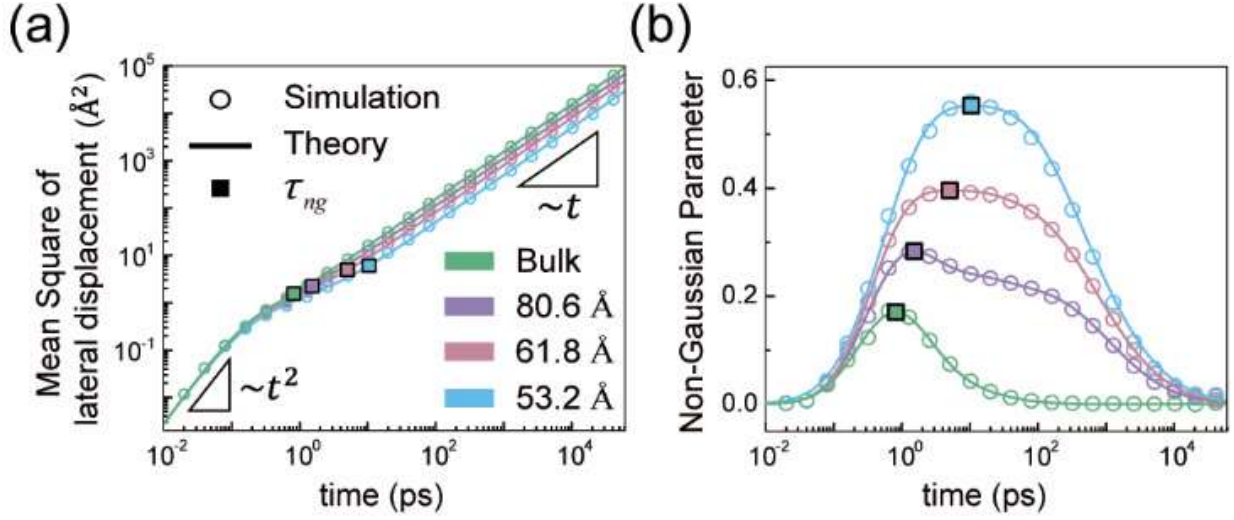
Figure 2. (a) Mean square displacement (MSD) and (b) non-Gaussian parameter (NGP) associated with the lateral displacement of water molecules for systems with various intermembrane separations: (circles) simulation results; (solid lines) eq S19 for MSD and eq S21 for NGP; (square) the NGP peak time (τ_{ng})

Our MD simulation study reveals that both the NGP peak time and the peak height increase as the separation, ℓ, between the membranes decreases (Figure 2b). A longer peak time and a greater peak height of the NGP signify, respectively, prolonged trapping of water molecules[23,27] and increased fluctuation in the lateral diffusion coefficient (see eq 4b). These phenomena can be attributed to the attractive interactions between interfacial water molecules and the functional groups in the lipid molecules. As ℓ decreases, the proportion of the trapped interfacial water molecules grows, leading to a decrease in the mean lateral diffusion coefficient and an increase in the variance of the diffusion coefficient.

At times longer than the NGP peak time, the nanoconfined molecules undergo Fickian yet non-Gaussian diffusion, with the NGP value decreasing with time. The nanoconfined water molecules have a far greater NGP value than bulk water molecules. The NGP of bulk water molecules becomes negligible at times longer than 10 ps; in contrast, the NGP of the nanoconfined water molecules does not vanish at times longer than 10 ns. The NGP shows a strongly non-exponential relaxation dynamics, whose time profile can be quantitatively explained by eqs 4b and 5 as shown later in this Letter.

We then identify the interfacial region where water molecules directly interact with the lipid head groups. For this purpose, we investigate the structure and dynamics of water molecules near the lipid-bilayers using the MD simulations. Figures 3a and 3b show the z-dependence of the density profile, $\rho(z)$, and the dipole orientation profile, $\langle \cos\theta \rangle_z$, of the nanoconfined water. Here, θ and bracket $\langle \cdots \rangle_z$ denote the angle between the water dipole moment and the z-axis and the average over water molecules located within an interval (z–0.25 Å, z+0.25 Å), respectively. As shown in Figure 3a, the water molecules in close vicinity of the membrane exhibit a lower density compared to the density, $\rho_{bulk}^{45°C} = 0.99$ g·cm^{-3}, of bulk water[28]. The dipole orientation profile, $\langle \cos\theta \rangle_z$, does not vanish for water molecules in the vicinity of the functional groups in the lipid molecules. This results from the non-isotropic interactions between the water molecules and those functional groups, whose positions along the z-direction are shown in Figure 3a. At positions near $z \cong 20$ Å, $\langle \cos\theta \rangle_z$ has a negative value, while at positions near $z \cong \ell - 20$ Å, it has a positive value, indicating that the water dipole moment tends to point toward phosphate and carbonyl groups rather than choline groups[7,8]. This is because water molecules in the vicinity of phosphate and carbonyl groups experience strong restrictions on their orientations due to the hydrogen

bonding with these groups, whereas those near choline groups exhibit broadly distributed angle distribution, forming the clathrate-like hydration shell around the choline groups[4,13].
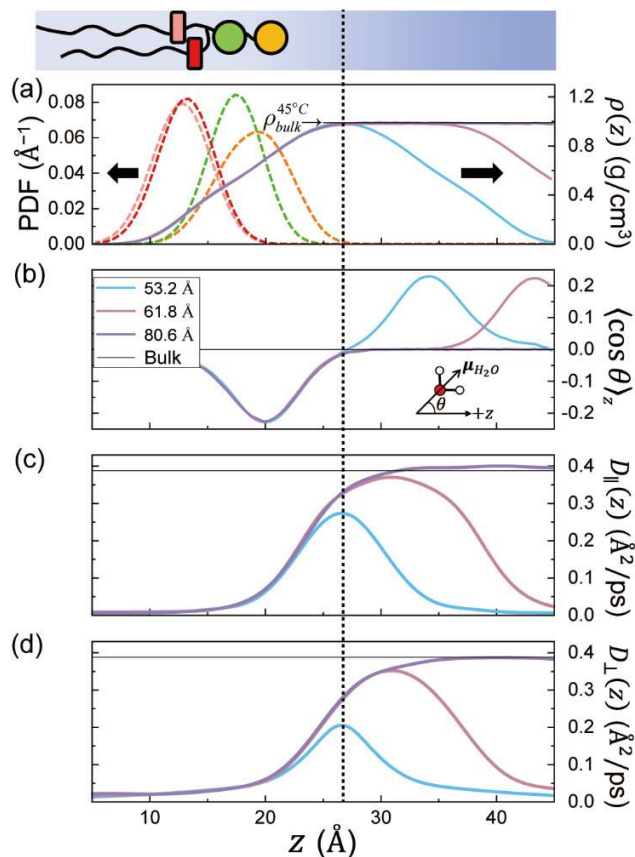
Figure 3. Dependence of structural and dynamical properties of the water molecules on the distance z from the center of the lipid membrane in the left. z-dependent profile of (a) mass density, $\rho(z)$, (b) orientation $\langle \cos\theta \rangle_z$, (c) lateral diffusion coefficient, $D_{\parallel}(z)$, and (d) longitudinal diffusion coefficient, $D_{\perp}(z)$, of water molecules. θ designates the angle between the water moment and the longitudinal axis. (dotted line) the position of the boundary, $z_c = 26.6$ Å, between interfacial water region and bulk-like water region. (dashed lines) probability distribution of the positions of various functional groups in the DMPC: (orange) the nitrogen atom in the choline group; (green) phosphorus atom in the phosphate group; (red and pink) the oxygen atoms in the

two carbonyl groups. The probability distribution of these functional groups as well as the z-dependent profiles of $\rho(z)$ and $\langle\cos\theta\rangle_z$ are largely independent of the intermembrane separation.

Remarkably, the density and dipole orientation profiles show little dependence on ℓ for the interfacial water molecules at z smaller than $z_c = 26.6$ Å but recover their respective bulk-limit values in the intermediate region defined by $z_c \leq z \leq \ell - z_c$. Based on these observations, we define z_c as the boundary between the interfacial water region and the bulk-like water region. The value of z_c (= 26.6 Å) estimated from our MD simulation is found to be comparable to the previously reported z_c values, 24 Å and 28 Å, which were estimated by investigating the structural order[15] and the rotational dynamics[19] of water molecules near the lipid membrane.

The diffusion coefficients of water molecules are also strongly dependent on their distance from the membrane. We obtain the z-dependent profiles of $D_{\parallel}(z)$ and $D_{\perp}(z)$ (Figures 3c and 3d) using umbrella sampling and mean first passage time analysis (Figures S1 and S2), respectively[14,29]. Within the interfacial water region ($z < z_c$), both the diffusion coefficients increase with z, and their z-dependent profiles are also similar across various intermembrane separations. For the system with $\ell = 80.6$ Å, both diffusion coefficients recover the bulk-limit value, $D_{bulk}^{45°C} = 3.88\times10^{-1}$ Å$^2\cdot$ps^{-1}, of the SPC/E water at distances greater than z_c. However, for the systems with $\ell < 80.6$ Å, the values of $D_{\parallel}(z)$ and $D_{\perp}(z)$ are smaller than $D_{bulk}^{45°C}$ across the entire z region. For example, when the value of ℓ is 53.2 Å, the maximum values of $D_{\parallel}(\ell/2)$ and $D_{\perp}(\ell/2)$ are only about 70% and 50% of $D_{bulk}^{45°C}$, respectively. Noting that the longitudinal position, z, of the central nitrogen atom in the choline group is about 19.3 $\pm$ 4 Å (Figure 3a), these results suggest that the

choline group in the lipid molecule retard the translational motion of water molecules located beyond its first hydration shell, which extends about 4.5 Å from the central nitrogen atom in the choline group[13].

The z-dependence profiles of water density $\rho(z)$ and the diffusion coefficients, $D_{\parallel}(z)$ and $D_{\perp}(z)$, are related to the time profile of $\eta_D^2\phi_D(t)$ and the NGP according to eqs 4b and 5. Equation 4b tells us that, after the onset of Fickian diffusion, the NGP time profile is completely determined by the mean-scaled TCF, $\eta_D^2\phi_D(t)\left[=\langle\delta D_{\parallel}(t)\delta D_{\parallel}(0)\rangle\big/\langle D_{\parallel}\rangle^2\right]$, of the diffusion coefficient fluctuation. Here, $\eta_D^2\left[=\langle D_{\parallel}^2\rangle\big/\langle D_{\parallel}\rangle^2-1\right]$ can be calculated from $D_{\parallel}(z)$ and $\rho(z)$ by using $\langle D_{\parallel}^n\rangle=\int_0^{\ell}dzD_{\parallel}^n(z)P_{eq}(z)$ with $P_{eq}(z)=\rho(z)\big/\int_0^{\ell}dz\rho(z)$. $\phi_D(t)$ can also be calculated from eq 5, where the Green's function $G_{SM}(z,t\,|\,z_0)$ is obtained by solving $\partial_t G_{SM}(z,t\,|\,z_0)=\partial_z[D_{\perp}(z)(\partial_z+\partial_z\beta U(z))]G_{SM}(z,t\,|\,z_0)$ with the initial condition $G_{SM}(z,0\,|\,z_0)=\delta(z-z_0)$. The thermal energy-scaled potential of mean force, $\beta U(z)$, can be estimated from $\rho(z)$ by $\beta U(z)=-\ln[\rho(z)\big/\rho_{bulk}^{45°C}]$. Across systems with various intermembrane separations, the result of $\eta_D^2\phi_D(t)$ calculated using our theory closely matches the long-time profile of $C_D(t)$ directly extracted from the MD simulation results (Figure 4a). In addition, the NGP time profiles calculated from eq 4b are also in quantitative agreement with the MD simulation results (Figure 4b). Furthermore, our theory predicts the lateral displacement distribution with a unimodal peak and a non-Gaussian tail for nanoconfined water molecules. We find the prediction of our theory in excellent agreement with the MD simulation results for the time-dependent lateral displacement distribution of water molecules at various times and separations between the membranes (Figure 4c). The agreement between theory and simulation again demonstrates the validity of our

assumption underlying eq 1, that is, the most important variable that affects the lateral thermal motion of an interfacial water molecule is the distance, z, between a water molecule and the center of the membrane.
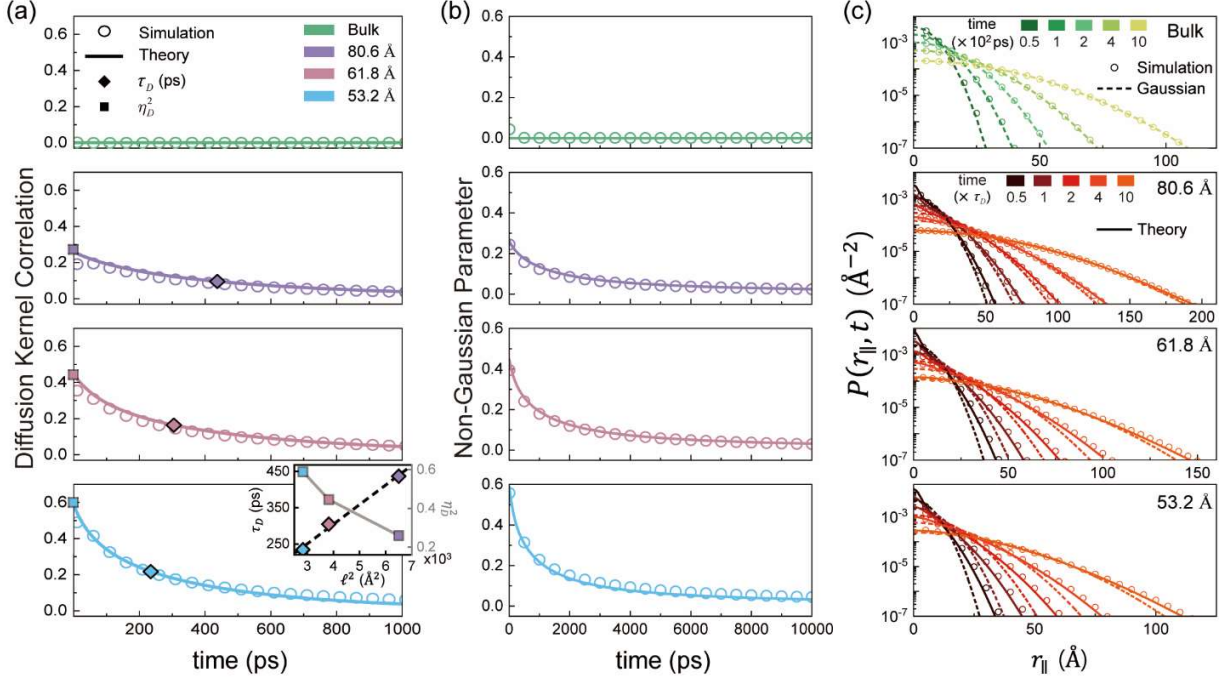
Figure 4. Diffusion Kernel Correlation, Non-Gaussian Parameter, and Lateral Displacement Distribution of water molecules confined between two lipid membranes with various intermembrane separations. (a) Comparison between the diffusion kernel correlation and the mean-scaled time correlation function of the lateral diffusion coefficient fluctuation: (circles) Diffusion Kernel Correlation, $C_{\mathcal{D}}(t)$, from the MD simulation results; (solid lines) mean-scaled TCFs, $\eta_D^2 \phi_D(t)$, of the lateral diffusion coefficient fluctuation calculated by eq 5; (diamond) relaxation time τ_D defined by $\phi_D(\tau_D) = e^{-1}$; (square) the value of the relative variance, η_D^2, of the diffusion coefficient. (Inset in (a)) Dependence of τ_D and η_D^2 on the square, ℓ^2, of intermembrane separation. (b) Non-Gaussian parameter $\alpha_2(t)$: (circles) simulation; (solid line) eq 4b. (c) Lateral

displacement distributions at various times: (circles) simulation results; (solid lines) theoretical predictions; (dotted line) Gaussian with zero mean and variance given by $4\langle D_\parallel \rangle t$.

The relaxation time τ_D of $\phi_D(t)$, defined by $\phi_D(\tau_D) = e^{-1}$, quadratically increases with the intermembrane separation ℓ (see inset of Figure 4a). This follows because, for the complete relaxation of the diffusion coefficient fluctuation, water molecules must travel the entire intermembrane space, and the time taken for this process should be proportional to the mean first passage time, which quadratically increases with ℓ (Movie S1). On the other hand, η_D^2 decreases with ℓ. This is because, as ℓ increases, the proportion of the trapped interfacial water molecules decreases, which leads to an increase in the mean lateral diffusion coefficient and a decrease in the variance of the diffusion coefficient.

We note here that, at times shorter than 0.1 ps, the NGP increases with time, which cannot be explained by eq 4b. At such short times, the DKC can be approximated by $C_{\mathcal{D}}(t)$ $\cong 2\left[\langle \mathcal{D}_\parallel(t) \rangle / \langle \mathcal{D}_\parallel(0) \rangle\right]^2 = 2\phi_v^2(t)$ (see the Figure S3a in the Supporting Information), where $\phi_v(t)$ denotes the normalized VAF of water molecules. Using this approximation in eq 2, we obtained the following short-time asymptotic expression of the NGP as

$$\alpha_2(t) = \frac{1}{18}\left(\gamma^2 - \mu\right)t^2 + \mathcal{O}(t^3),\tag{6}$$

where γ and μ denote $-\lim_{t\to 0}\partial\phi_v(t)/\partial t$ and $\lim_{t\to 0}\partial^2\phi_v(t)/\partial t^2$, respectively. Explicit expressions of γ and μ are available for our model (see the paragraph below eq S24 in the Supporting

Information). According to this result, the NGP quadratically increases with time, which quantitatively explains our simulation results for the short-time asymptotic behavior of the NGP.

The major contributor to the short-time dynamics of the NGP is the relaxation dynamics of the velocity fluctuation, and the two-time velocity auto-correlation function completely determines the NGP time profile. After the onset of Fickian diffusion, however, the relaxation dynamics of the diffusion coefficient fluctuation additionally contributes to the NGP time profile. For bulk water system, where the diffusion coefficient fluctuation is negligible, the short-time asymptotic expression of the NGP that only accounts for the velocity relaxation provides a quantitative explanation of the long-time relaxation of the NGP as well as the short-time relaxation (see the Figure S3b in the Supporting Information).

We present a physical model and transport equation that quantitatively explain the stochastic thermal motion of water molecules in intermembrane space. The lateral displacement distribution of the water molecules nanoconfined between two membranes strongly deviates from Gaussian, which originates from dynamic fluctuation in the lateral diffusion coefficient. This fluctuation occurs because the lateral diffusion coefficient of a water molecule primarily depends on its distance from the membrane center, and this distance fluctuates over time, owing to thermal motion of the water molecule in the longitudinal direction. In addition, using the molecular dynamics (MD) simulation, we investigate the dependence of the mass density, the orientation, and the lateral and longitudinal diffusion coefficients of a water molecule nanoconfined between two phospholipid membranes on its distance from the phospholipid membrane center. This study shows the presence of interfacial region within 26.6 Å from the membrane center. Water molecules in the interfacial region have a structure and dynamics far different from bulk water molecules. The properties of interfacial water molecules are robust with respect to changes in intermembrane

separation. Our theory provides a unified, quantitative explanation of our MD simulation results for the mean square displacement, non-Gaussian parameter, and displacement distribution of nanoconfined water molecules. Our model is applicable or can be extended to quantitative investigation into the dynamics of transport and transport-coupled processes occurring in various nanoconfined environments.

ASSOCIATED CONTENT

Supporting Information

Movie S1: Heatmap of discrete Green's function (MP4)

Additional figures, tables, computational details for MD simulation and captions for Movie S1 (PDF)

(link: https://doi.org/10.1021/acs.jpclett.4c00323)

REFERENCES

(1)   Demirel, Y.; Gerbaud, V. Chapter 11 - Thermodynamics and Biological Systems. In *Nonequilibrium Thermodynamics (Fourth Edition)*; Elsevier, 2019; pp 489–571.

(2)   McCann, F. E.; Vanherberghen, B.; Eleme, K.; Carlin, L. M.; Newsam, R. J.; Goulding, D.; Davis, D. M. The Size of the Synaptic Cleft and Distinct Distributions of Filamentous Actin, Ezrin, CD43, and CD45 at Activating and Inhibitory Human NK Cell Immune Synapses. *J. Immunol.* **2003**, *170* (6), 2862–2870.

(3)   Terasaki, M.; Shemesh, T.; Kasthuri, N.; Klemm, R. W.; Schalek, R.; Hayworth, K. J.; Hand, A. R.; Yankova, M.; Huber, G.; Lichtman, J. W.; Rapoport, T. A.; Kozlov, M. M. Stacked Endoplasmic Reticulum Sheets Are Connected by Helicoidal Membrane Motifs. *Cell* **2013**, *154* (2), 285–296.

(4)   Zhao, W.; Moilanen, D. E.; Fenn, E. E.; Fayer, M. D. Water at the Surfaces of Aligned Phospholipid Multibilayer Model Membranes Probed with Ultrafast Vibrational Spectroscopy. *J. Am. Chem. Soc.* **2008**, *130* (42), 13927–13937.

(5)   Kundu, A.; Kwak, K.; Cho, M. Water Structure at the Lipid Multibilayer Surface: Anionic Versus Cationic Head Group Effects. *J. Phys. Chem. B* **2016**, *120* (22), 5002–5007.

(6)   Kundu, A.; Błasiak, B.; Lim, J.-H.; Kwak, K.; Cho, M. Water Hydrogen-Bonding Network Structure and Dynamics at Phospholipid Multibilayer Surface: Femtosecond Mid-IR Pump–Probe Spectroscopy. *J. Phys. Chem. Lett.* **2016**, *7* (5), 741–745.

(7)   Mondal, J. A.; Nihonyanagi, S.; Yamaguchi, S.; Tahara, T. Three Distinct Water Structures at a Zwitterionic Lipid/Water Interface Revealed by Heterodyne-Detected Vibrational Sum Frequency Generation. *J. Am. Chem. Soc.* **2012**, *134* (18), 7842–7850.

(8)   Dreier, L. B.; Wolde-Kidan, A.; Bonthuis, D. J.; Netz, R. R.; Backus, E. H. G.; Bonn, M. Unraveling the Origin of the Apparent Charge of Zwitterionic Lipid Layers. *J. Phys. Chem. Lett.* **2019**, *10* (20), 6355–6359.

(9)   Zhang, R.; Cross, T. A.; Peng, X.; Fu, R. Surprising Rigidity of Functionally Important Water Molecules Buried in the Lipid Headgroup Region. *J. Am. Chem. Soc.* **2022**, *144* (17), 7881–7888.

(10)   Kazoe, Y.; Mawatari, K.; Li, L.; Emon, H.; Miyawaki, N.; Chinen, H.; Morikawa, K.; Yoshizaki, A.; Dittrich, P. S.; Kitamori, T. Lipid Bilayer-Modified Nanofluidic Channels of Sizes with Hundreds of Nanometers for Characterization of Confined Water and Molecular/Ion Transport. *J. Phys. Chem. Lett.* **2020**, *11* (14), 5756–5762.

(11)   Saruko, T.; Morikawa, K.; Kitamori, T.; Mawatari, K. Proton Diffusion and Hydrolysis Enzymatic Reaction in 100 Nm Scale Biomimetic Nanochannels. *Biomicrofluidics* **2022**, *16* (4), 044109.

(12) Kazoe, Y.; Ikeda, K.; Mino, K.; Morikawa, K.; Mawatari, K.; Kitamori, T. Quantitative Characterization of Liquids Flowing in Geometrically Controlled Sub-100 nm Nanofluidic Channels. *Anal. Sci.* **2023**.

(13) Lee, E.; Kundu, A.; Jeon, J.; Cho, M. Water Hydrogen-Bonding Structure and Dynamics near Lipid Multibilayer Surface: Molecular Dynamics Simulation Study with Direct Experimental Comparison. *J. Chem. Phys.* **2019**, *151* (11), 114705.

(14) von Hansen, Y.; Gekle, S.; Netz, R. R. Anomalous Anisotropic Diffusion Dynamics of Hydration Water at Lipid Membranes. *Phys. Rev. Lett.* **2013**, *111* (11), 118103.

(15) Martelli, F.; Crain, J.; Franzese, G. Network Topology in Water Nanoconfined between Phospholipid Membranes. *ACS Nano* **2020**, *14* (7), 8616–8623.

(16) Högberg, C.-J.; Lyubartsev, A. P. A Molecular Dynamics Investigation of the Influence of Hydration and Temperature on Structural and Dynamical Properties of a Dimyristoylphosphatidylcholine Bilayer. *J. Phys. Chem. B* **2006**, *110* (29), 14326–14336.

(17) Yamamoto, E.; Akimoto, T.; Hirano, Y.; Yasui, M.; Yasuoka, K. Power-Law Trapping of Water Molecules on the Lipid-Membrane Surface Induces Water Retardation. *Phys. Rev. E* **2013**, *87* (5), 052715.

(18) Hansen, F. Y.; Peters, G. H.; Taub, H.; Miskowiec, A. Diffusion of Water and Selected Atoms in DMPC Lipid Bilayer Membranes. *J. Chem. Phys.* **2012**, *137* (20), 204910.

(19) Martelli, F.; Ko, H.-Y.; Borallo, C. C.; Franzese, G. Structural Properties of Water Confined by Phospholipid Membranes. *Front. Phys.* **2017**, *13* (1), 136801.

(20) Malik, S.; Debnath, A. Dehydration Induced Dynamical Heterogeneity and Ordering Mechanism of Lipid Bilayers. *J. Chem. Phys.* **2021**, *154* (17), 174904.

(21) Calero, C.; Stanley, H.; Franzese, G. Structural Interpretation of the Large Slowdown of Water Dynamics at Stacked Phospholipid Membranes for Decreasing Hydration Level: All-Atom Molecular Dynamics. *Materials* **2016**, *9* (5), 319.

(22) Wang, B.; Kuo, J.; Bae, S. C.; Granick, S. When Brownian Diffusion Is Not Gaussian. *Nat. Mater.* **2012**, *11* (6), 481–485.

(23) Song, S.; Park, S. J.; Kim, M.; Kim, J. S.; Sung, B. J.; Lee, S.; Kim, J.-H.; Sung, J. Transport Dynamics of Complex Fluids. *Proc. Natl. Acad. Sci. U.S.A.* **2019**, *116* (26), 12733–12742.

(24) Rahman, A.; Singwi, K. S.; Sjölander, A. Theory of Slow Neutron Scattering by Liquids. I. *Phys. Rev.* **1962**, *126* (3), 986–996.

(25) Rahman, A. Correlations in the Motion of Atoms in Liquid Argon. *Phys. Rev.* **1964**, *136* (2A), A405-A411.

(26) Dickson, C. J.; Madej, B. D.; Skjevik, Å. A.; Betz, R. M.; Teigen, K.; Gould, I. R.; Walker, R. C. Lipid14: The Amber Lipid Force Field. *J. Chem. Theory Comput.* **2014**, *10* (2), 865–879.

(27) Odagaki, T.; Hiwatari, Y. Gaussian–to–Non-Gaussian Transition in Supercooled Fluids. *Phys. Rev. A* **1991**, *43* (2), 1103–1106.

(28) Wagner, W.; Pruß, A. The IAPWS Formulation 1995 for the Thermodynamic Properties of Ordinary Water Substance for General and Scientific Use. *J. Phys. Chem. Ref. Data* **2002**, *31* (2), 387–535.

(29) Szabo, A.; Schulten, K.; Schulten, Z. First Passage Time Approach to Diffusion Controlled Reactions. *J. Chem. Phys.* **1980**, *72* (8), 4350–4357.

2 **Transport Dynamics of Water Molecules**

3 **Confined between Lipid Membranes**

4 Minho Lee[1, 2], Euihyun Lee[3], Ji-Hyun Kim[1, 2], Hyonseok Hwang[6], Minhaeng Cho[4, 5*], and Jaeyoung Sung[1, 2*]

5 *[1] Creative Research Initiative Center for Chemical Dynamics in Living Cells, Chung-Ang University, Seoul*

6 *06974, Republic of Korea*

7 *[2] Department of Chemistry, Chung-Ang University, Seoul 06974, Republic of Korea*

8 *[3] Department of Chemistry, The University of Texas at Austin, TX 78757, USA*

9 *[4] Center for Molecular Spectroscopy and Dynamics, Institute for Basic Science (IBS), Seoul 02841, Republic of*

10 *Korea*

11 *[5] Department of Chemistry, Korea University, Seoul 02841, Republic of Korea*

12 *[6] Department of Chemistry, Institute for Molecular Science and Fusion Technology, Kangwon National*

13 *University, Chuncheon, Gangwon-do 24341, Republic of Korea*

14 Corresponding authors: jaeyoung@cau.ac.kr (J.S.), mcho@korea.ac.kr (M.C.)

Table of contents

Supplementary Text S1: Computational details of molecular dynamics simulations

Molecular Dynamics (MD) simulations were carried out using the AMBER 21 program package. We constructed simulation systems composed of 128 DMPC (1,2-dimyristoyl-sn-glycero-3-phosphocholine) lipids and a various number, 2560, 3840, and 6400 of water molecules, using the CHARMM-GUI membrane builder tool[1–6]. The force field parameters of DMPC and water molecules were replaced with the AMBER lipid 14[7] and SPC/E, respectively. Similarly, an MD simulation system for pure water, which is composed of 5,000 water molecules, was constructed using CHARMM-GUI solution builder[1,2,6], and the MD simulation was carried out using the same SPC/E force field. Periodic boundary conditions were applied to both the pure water and the lipid bilayer systems. In the case of the pure water system, our pure water model system with the periodic boundary conditions serves as a realistic and reliable representation of bulk water without edge effects. For the lipid bilayer system, our periodic boundary conditions effectively confine the water molecules within the lipid membranes. The particle mesh Ewald method[8] was used to calculate long-range electrostatic interactions, and the cutoff distance of 10 Å was used to calculate the Lennard-Jones interaction and the real space part of the Ewald sum. A time step of our MD simulations was set to 1 fs.

Before obtaining the simulation trajectories of the NVT ensemble of our systems, we conducted an equilibration procedure. For the pure water simulation, the initial configuration of water molecules was first stabilized through energy minimization for 5,000 steps, employing both the steepest descent method and the conjugate gradient method. This was followed by a 2 ns constant NpT equilibration at 1.0 atm and 318 K, using isotropic position scaling with a relaxation time of 2 ps. For temperature control, the Langevin thermostat, with a collision frequency of 1.0 ps^{-1}, was utilized. Subsequently, a 2 ns constant NVT simulation at 318 K was

52 carried out, using the Langevin thermostat to ensure that the system relaxed to the thermal

53 equilibrium state. Regarding the DMPC lipid bilayer system simulation, the initial

54 configuration of the system underwent a 10,000-step energy minimization using both the

55 steepest descent method and the conjugate gradient method. Then, the system was rapidly

56 heated from 0 K to 100 K over 40 ps, using the Langevin thermostat with a collision frequency

57 of 1.0 ps^{-1} and weak restraints on the lipid molecules with a force constant of 10. kcal mol^{-1}

58 Å^{-2}. Subsequently, a gradual heating from 100 K to 318 K over 2 ns was performed with the

59 same thermostat setting and restraints. After the heating process, a 50 ns *NpT* simulation was

60 carried out at 318 K, using the Langevin thermostat with anisotropic pressure scaling (1 atm)

61 without restraining lipids. From the results of the last process, the values of the separation, ℓ,

62 between two lipid membranes, i.e., system box length along the perpendicular direction to the

63 membrane surface, were determined. The values of the intermembrane separations, ℓ, are 53.2

64 Å, 61.8 Å, and 80.6 Å for our DMPC lipids simulation systems containing 2560, 3840, and

65 6400 water molecules, respectively.

66 After the equilibration procedure, production runs were carried out for our systems at 318

67 K under constant *NVT* conditions with the following procedures:

68 (1) To calculate the mean square displacement (MSD) and non-Gaussian parameter (NGP)

69   for the lateral displacement of water molecules, shown in Figure 2, we conducted the

70   MD simulation for each system using two different recording time intervals. The

71   simulation trajectories were recorded every 10 fs for the first 1 ns-long *NVT*

72   simulations to investigate the short-time dynamics of water molecules. Afterward, the

73   trajectories were saved every 10 ps over the following 99 ns-long *NVT* simulation to

74   investigate the long-time dynamics of the system. This 1 ns-long NVT simulations

75   were repeated seven times for each intermembrane separation of our system.

76   (2) To obtain the z-dependent profile of the lateral diffusion coefficient, $D_{\parallel}(z)$, shown in

77   Figure S1, we conducted additional simulation runs using umbrella sampling. The

78   simulation trajectories were recorded at every 10 ps during the 1 μs-long *NVT*

79   simulations. A more detailed description of this simulation process is presented in the

80   caption of Figure S1.

81   (3) To obtain the z-dependent profile, the longitudinal diffusion coefficient, $D_{\perp}(z)$,

82   profiles shown in Figure S2, using the method presented in Ref.[9–11], we conducted

83   another set of simulations where the simulation trajectories were saved at intervals of

84   1 ps for the 1 μs-long *NVT* simulations. A more detailed description of this simulation

85   is presented in the caption of Figure S2.

Supplementary Text S2: Derivation of analytic expressions for the MSD and NGP

Let us first obtain the analytic expression for the second and fourth moments of the lateral displacement of water molecules in the intermembrane space, starting from eq 1. On the left-hand-side of eq 1, $\hat{\dot{p}}(\mathbf{r}_\parallel, z, s)$ can be replaced by $\hat{\dot{p}}(\mathbf{r}_\parallel, z, s) = s\hat{p}(\mathbf{r}_\parallel, z, s) - p(\mathbf{r}_\parallel, z, 0)$. Here, $p(\mathbf{r}_\parallel, z, 0)$ denotes the initial condition of the joint probability density, given by $p(\mathbf{r}_\parallel, z, 0) = \delta(\mathbf{r}_\parallel - \mathbf{r}_{\parallel,0}) P_{eq}(z)$, where, $\mathbf{r}_{\parallel,0}$ and $P_{eq}(z)$ denote the initial lateral position vector and the equilibrium distribution of water molecule along the z-axis, respectively. When $\mathbf{r}_{\parallel,0}$ is chosen to be the origin of our coordinate, i.e., $\mathbf{r}_{\parallel,0} = \mathbf{0}$, $\mathbf{r}_\parallel$ represents the displacement vector. By taking the Fourier transform of eq 1, we obtain

$$\hat{\tilde{\dot{p}}}(\mathbf{k}_\parallel, z, s) = s\hat{\tilde{p}}(\mathbf{k}_\parallel, z, s) - P_{eq}(z) = -\hat{\mathcal{D}}_\parallel(z, s)k_\parallel^2 \hat{\tilde{p}}(\mathbf{k}_\parallel, z, s) + L(z)\hat{\tilde{p}}(\mathbf{k}_\parallel, z, s). \tag{S1}$$

Here, $\hat{\tilde{p}}(\mathbf{k}_\parallel, z, s)$ and $k_\parallel$ represent the Fourier transformation of $\hat{p}(\mathbf{r}_\parallel, z, s)$, defined by $\hat{\tilde{p}}(\mathbf{k}_\parallel, z, s) = \int_0^\infty d\mathbf{r}_\parallel e^{i\mathbf{k}_\parallel \cdot \mathbf{r}_\parallel} \hat{p}(\mathbf{r}_\parallel, z, s)$, and the magnitude of the wave vector, $\mathbf{k}_\parallel$, i.e. $k_\parallel = |\mathbf{k}_\parallel|$, respectively.

The first two non-vanishing moments, $\Delta_2(t) \left[\equiv \langle \Delta \mathbf{r}_\parallel(t)^2 \rangle\right]$ and $\Delta_4(t) \left[\equiv \langle \Delta \mathbf{r}_\parallel(t)^4 \rangle\right]$, of the distribution of the lateral displacement $\Delta \mathbf{r}_\parallel(t) \left[\equiv \mathbf{r}_\parallel(t) - \mathbf{r}_\parallel(0)\right]$ are related to z-dependent displacement distribution, $p(\mathbf{r}_\parallel, z, t)$, by

$$\Delta_n(t) = \int_0^\ell dz \int d\mathbf{r}_\parallel (r_\parallel)^n p(\mathbf{r}_\parallel, z, t) = \int_0^\ell dz \Delta_n(z, t), \tag{S2}$$

104   where $\Delta_n(z,t)$ is defined by $\Delta_n(z,t) = \int d\mathbf{r}_{\parallel} \, (r_{\parallel})^n \, p(\mathbf{r}_{\parallel}, z, t) = 2\pi \int_0^{\infty} dr_{\parallel} \, (r_{\parallel})^{n+1} \, p(\mathbf{r}_{\parallel}, z, t)$. The

105   expression of $\Delta_n(z,t)$ can be obtained by the second and fourth derivatives of $\tilde{p}(\mathbf{k}_{\parallel}, z, t)$

106   with respect to $k_{\parallel}$ and setting $k_{\parallel} = 0$ in the resulting equation, that is,

$$
\begin{aligned}
\partial_{k_{\parallel}}^q \tilde{p}(k_{\parallel}, z, t)\Big|_{k_{\parallel}=0} &= \partial_{k_{\parallel}}^q \int d\mathbf{r}_{\parallel} \, e^{ik_{\parallel} r_{\parallel} \cos\theta} \, \tilde{p}(\mathbf{r}_{\parallel}, z, t)\Big|_{k_{\parallel}=0} \\
&= i^q \int d\mathbf{r}_{\parallel} \Big[\big(r_{\parallel} \cos\theta\big)^q \, \tilde{p}(\mathbf{r}_{\parallel}, z, t)\Big] \\
&= i^q \int_0^{\infty} dr_{\parallel} \int_0^{2\pi} d\theta \, r_{\parallel} \Big[\big(r_{\parallel} \cos\theta\big)^q \, \tilde{p}(\mathbf{r}_{\parallel}, z, t)\Big] \\
&= \begin{cases} -\Delta_2(z,t)/2, & \text{for } q = 2 \\ 3\Delta_4(z,t)/8, & \text{for } q = 4 \end{cases}
\end{aligned}
\tag{S3}
$$

108   where θ denotes the angle between the two vectors, $\mathbf{k}_{\parallel}$ and $\mathbf{r}_{\parallel}$, defined by

109      $\cos\theta = \mathbf{k}_{\parallel} \cdot \mathbf{r}_{\parallel} / (k_{\parallel} r_{\parallel})$. Taking the mathematical operation, $\partial_{k_{\parallel}}^2 (...)_{k_{\parallel}=0}$, on both sides of eq S1

110   and using eq S3, we obtain

$$
\hat{\Delta}_2(z,s) = 4\big(s - L(z)\big)^{-1} \hat{\mathcal{D}}_{\parallel}(z,s) P_{eq}(z) / s .
\tag{S4}
$$

112   Equation S4 can be written as

$$
\hat{\Delta}_2(z,s) = 4 \int_0^{\ell} dz_0 \, \hat{G}(z,s \,|\, z_0) \hat{\mathcal{D}}_{\parallel}(z_0, s) P_{eq}(z_0) / s .
\tag{S5}
$$

114   where $\hat{G}(z,s\,|\,z_0)\Big[= \big(s - L(z)\big)^{-1} \delta(z - z_0)\Big]$ denotes the Laplace transform of Green's function

115      $G(z,t\,|\,z_0)$ defined by $\partial_t G(z,t\,|\,z_0) = L(z) G(z,t\,|\,z_0)$, with the initial condition,

116      $G(z,0\,|\,z_0) = \delta(z - z_0)$. The Green's function represents the conditional probability that a water

117   molecule initially located at z_0 is found at z at time t. Integrating both sides of eq S5 over z,

118   and using the normalization condition, $\int_0^{\ell} dz \, G(z,t\,|\,z_0) = 1$, we obtain

119
$$\hat{\Delta}_2(s) = 4\langle\hat{\mathcal{D}}_\|(s)\rangle / s^2 . \tag{S6}$$

120   The analytic expression of $\Delta_4(t)$ can be obtained by following a similar line of

121   derivation. Taking the mathematical operation, $\partial_{k_\|}^4(...)_{k_\|=0}$, on both sides of eq S1 and using

122   eq S3, we obtain

123
$$\hat{\Delta}_4(z,s) = 64\int_0^\ell dz_1 \int_0^\ell dz_0 \hat{G}(z,s\,|\,z_1)\hat{\mathcal{D}}_\|(z_1,s)\hat{G}(z_1,s\,|\,z_0)\hat{\mathcal{D}}_\|(z_0,s)P_{eq}(z_0) / s . \tag{S7}$$

124   Integrating both sides of eq S7 over z, and using the normalization condition,

125    $\int_0^\ell dz\, G(z,t\,|\,z_0) = 1$, we obtain

126
$$\hat{\Delta}_4(s) = \frac{64}{s^3}\langle\hat{\mathcal{D}}_\|(s)\rangle^2\left(1 + s\,\hat{C}_\mathcal{D}(s)\right) = 4s\hat{\Delta}_2(s)^2\left(1 + s\,\hat{C}_\mathcal{D}(s)\right), \tag{S8}$$

127   where $C_\mathcal{D}(t)$ denotes the lateral diffusion kernel correlation (DKC) defined by

128
$$\hat{C}_\mathcal{D}(s) = \int_0^\ell dz \int_0^\ell dz_0 \frac{\delta\hat{\mathcal{D}}_\|(z,s)}{\langle\hat{\mathcal{D}}_\|(s)\rangle}\hat{G}(z,s\,|\,z_0)\frac{\delta\hat{\mathcal{D}}_\|(z_0,s)}{\langle\hat{\mathcal{D}}_\|(s)\rangle}P_{eq}(z_0) . \tag{S9}$$

129   Here, the lower and upper bounds, 0 and ℓ, of the integral denote the positions of two different

130   membrane centers. That is to say, ℓ denotes the separation between the two lipid membrane

131   centers (see Figure 1).

132   After the onset of Fickian diffusion, the MSD linearly increases with time because the

133   mean diffusion kernel, $\langle\mathcal{D}_\|(z,t)\rangle$, is negligibly small at the time scale of Fickian diffusion,

134   where we have $\Delta_2(t) = 4\int_0^t d\tau(t-\tau)\langle\mathcal{D}_\|(\tau)\rangle \cong 4t\int_0^\infty\langle\mathcal{D}_\|(\tau)\rangle$. After the onset of Fickian

135   diffusion, the diffusion kernel, $\hat{\mathcal{D}}_\|(z,s)$, can be replaced by its small-s limit value, $\hat{\mathcal{D}}_\|(z,0)$,

136   which is nothing but the lateral diffusion coefficient, $D_\|(z)$, of water molecules at longitudinal

position z. Additionally, after the onset of Fickian diffusion , $L(z)$ in eq 1 can be approximated by the Smoluchowski operator, defined as, $L_{SM}(z) = \partial_z[D_\perp(z)(\partial_z + \partial_z \beta U(z))]$. Here, $D_\perp(z)$ and $\beta U(z)$ respectively denote the z-dependent diffusion coefficient associated with the thermal motion of water molecules in the longitudinal direction and the thermal energy-scaled potential of mean force. Throughout β denotes $\beta = 1/k_B T$ where k_B and T denote the Boltzmann constant and temperature, respectively. Therefore, at the time scales of Fickian diffusion, the exact expression of the first two non-vanishing moments, eqs S6 and S8, can be approximated as

$$\Delta_2(t) = 4\langle D_\parallel \rangle \rangle t, \tag{S10}$$

$$\Delta_4(t) = 32\langle D_\parallel \rangle^2 \left[t^2 + 2\eta_D^2 \int_0^t dt'(t-t')\phi_D(t') \right]. \tag{S11}$$

Here, $\langle D_\parallel \rangle$ and $\eta_D^2 \left[= \langle \delta D_\parallel(z)^2 \rangle / \langle D_\parallel \rangle^2 \right]$ respectively denote, the mean diffusion coefficient and the relative variance of the z-dependent lateral diffusion coefficient. $\phi_D(t)$ represents the normalized time-correlation function (TCF) of the lateral diffusion coefficient fluctuation given by

$$\phi_D(t) = \frac{\langle \delta D_\parallel(t)\delta D_\parallel(0) \rangle}{\langle \delta D_\parallel^2 \rangle} = \langle \delta D_\parallel^2 \rangle^{-1} \int_0^\ell dz \int_0^\ell dz_0 \delta D_\parallel(z) G_{SM}(z,t \mid z_0) \delta D_\parallel(z_0) P_{eq}(z_0), \tag{S12}$$

where $G_{SM}(z,t \mid z_0)$ designates Green's function defined by $\partial_t G_{SM}(z,t \mid z_0)$ $= L_{SM}(z)G_{SM}(z,t \mid z_0)$, with the initial condition, $G_{SM}(z,0 \mid z_0) = \delta(z - z_0)$.

Substituting the eqs S10 and S11 into the definition of the NGP, $\alpha_2(t)$ $\left[\equiv \Delta_4(t) / (2\Delta_2(t)^2) - 1 \right]$, we obtain the analytical expressions of the NGP time profile as

$$\alpha_2(t) = \frac{2\eta_D^2}{t^2} \int_0^t dt'(t-t')\phi_D(t'). \tag{S13}$$

156

157   Equations S6, S8, S10, and S13 are equivalent to eqs 2a, 2b, 4a, and 4b in the main text,

158   respectively.

Figure S1: z-dependent profiles of lateral diffusion coefficient
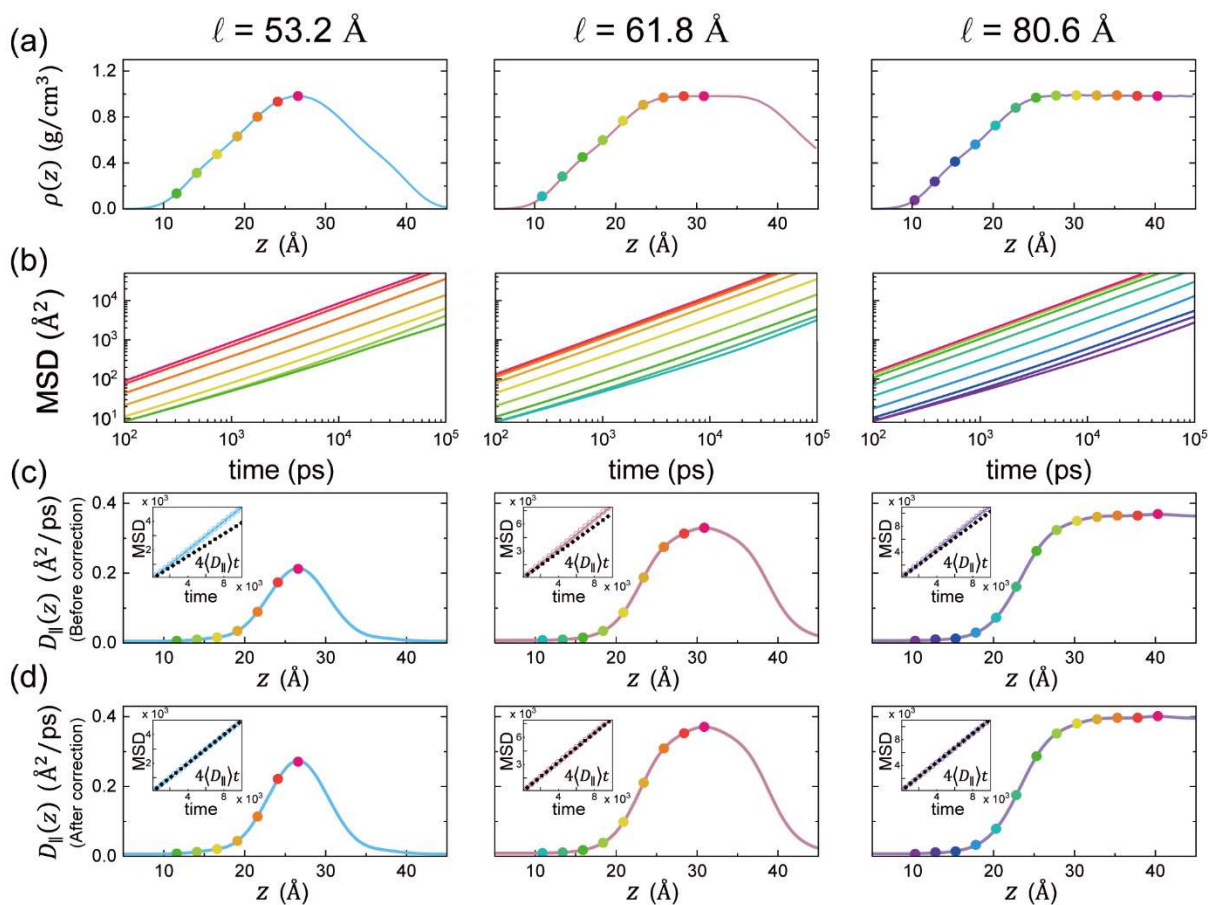
161   To determine the z-dependent profile of the lateral diffusion coefficient, we obtain the z-

162 dependence of the MSD of water molecules in the intermembrane space. For this purpose, we

163 estimate the MSD time profile of water molecules within each layer region defined by

164 $z_0 - 1.5\text{Å} \leq z \leq z_0 + 1.5\text{Å}$, systematically changing the center position z_0 of the layer. It is

165 difficult to estimate the long-time behavior of the MSD accurately, because very few water

166 molecules remain in the initial layer at long times[11]. To circumvent this difficulty, we employ

167 a constrained MD simulation in which we randomly choose approximately 10 % of water

168 molecules within a layer and apply Harmonic potential, $U(z) = k(z - z_0)^2$ to the chosen

169 water molecules. Here, k represents the spring constant whose value is set to be 1.25 [Kcal/(mol

S11

170 $\cdot\text{Å}^2)]$.

171   For the first round of our constrained simulation, we set the value of z_0 to be $\ell/2$. Then

172 we repeatedly perform the constrained simulation, systematically changing the value of z_0 by

173 2.5 Å, until we span the entire intermembrane space. The position of z_0 for each simulation

174 is represented by a colored dot in Figure S1a. In the constrained MD simulation, the MD

175 trajectories were recorded every 10 ps during 1μs-long *NVT* simulations. The number of water

176 molecules constrained by the harmonic potential is about 6% for each system, which amounts

177 to 403, 240, and 168 for the system with ℓ = 80.6 Å, 61.8 Å, and 53.2 Å.

178   From the trajectories of water molecules constrained by the harmonic potential, we

179 obtained the MSDs of the lateral water displacement for every layer of the simulation system

180 with different intermembrane separations (Figure S1b). Each solid line in Figure S1b represents

181 the MSD obtained from the constrained MD simulation with z_0 at the position marked by the

182 dot of the same color in Figure S1a. From the long-time MSD profile, we estimate the lateral

183 diffusion coefficient at each z position by $D_\parallel(z) = \lim_{t\to\infty} \Delta_2(z,t)/4t$. These values are shown

184 as circle symbols in Figure S1c. The resulting profile of the lateral diffusion coefficient can

185 well be fitted to the muti-Gaussian function,

186
$$D_\parallel(z) = y_0 + \sum_{i=1}^{n} \frac{a_i}{\omega_i\sqrt{\pi/2}} \exp\left(-2\left(\frac{z-z_{c,i}}{\omega_1}\right)^2\right), \tag{S14}$$

187 as shown as solid lines in Figure S1c. The optimized parameters for these fittings are provided

188 in Table S1. Using the multi-Gaussian representation of $D_\parallel(z)$, we calculate the mean lateral

189 diffusion coefficient, $\langle D_\parallel \rangle$, by

$$\langle D_\parallel \rangle = \int_0^\ell dz D_\parallel(z) P_{eq}(z) \tag{S15}$$

191   with $P_{eq}(z) = \rho(z) \Big/ \int_0^\ell dz \rho(z)$. Here, $\rho(z)$ denotes the mass density profile of water

192   molecules, shown in Figure S1a.

193   To test the accuracy of $D_\parallel(z)$ obtained from our constrained MD simulations, we

194   compared $4\langle D_\parallel \rangle t$ with the MSD obtained from the simulation of the entire system as shown

195   in insets of Figure S1c. These results clearly show that the estimation of $D_\parallel(z)$ and $\langle D_\parallel \rangle$

196   from our constrained MD simulation is not perfectly accurate. $\langle D_\parallel \rangle$ estimated from our

197   constrained MD simulation is slightly smaller than the true value of $\langle D_\parallel \rangle$ estimated from the

198   MSD of the entire system. This discrepancy is expected because 10% of the water molecules

199   are constrained in each layer by the fictitious harmonic potential, and their transport dynamics

200   would not be exactly the same as the transport dynamics of the free water molecules moving

201   across various layers.

202   We resolve this issue by introducing a correction factor, c, to $D_\parallel(z)$ estimated from our

203   constrained MD simulation in such a way that the mean lateral diffusion coefficient calculated

204   by $c \int_0^\ell dz D_\parallel(z) P_{eq}(z)$ is the same as the true value of $\langle D_\parallel \rangle$ estimated from the MSD of the

205   entire system (see insets of Figure S1d). The values of the correction factor are 1.087, 1.124,

206   and 1.276 for the systems with ℓ = 80.6 Å, 61.8 Å, and 53.2 Å, respectively. The value of the

207   corrected lateral diffusion coefficient, $c D_\parallel(z)$, are represented by solid lines in Figure S1d and

208   Figure 3c in the main text.

209   We use the corrected lateral diffusion coefficient profiles in calculating the theoretical

210   results depicted in Figure 4 of the main text. The agreement between our theoretical results and

211 the MD simulation results for the time profiles of the NGP, the TCF of the lateral diffusion

212 coefficient, and the lateral displacement distribution at various times confirms the accuracy of

213 our corrected lateral diffusion coefficient profiles.

Figure S2: z-dependent profiles of longitudinal diffusion coefficient
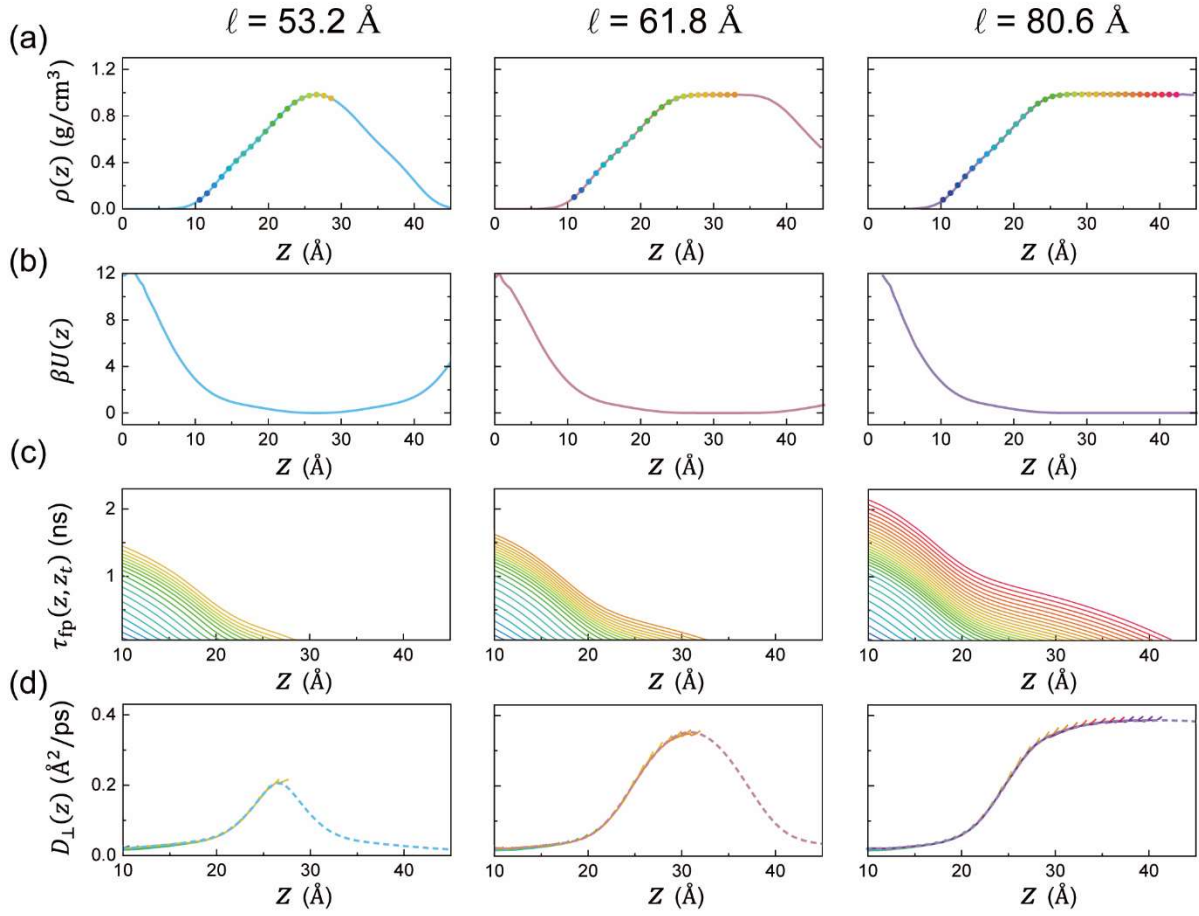
216   We obtain the longitudinal diffusion coefficient profile, $D_{\perp}(z)$, from the mean-first

217   passage time profile (MFPT), using the method developed in Ref.[9–11]. The MFPT, $\tau_{\mathrm{fp}}(z, z_t)$,

218   denotes the average time required for a water molecule initially located at z to arrive at a target

219   position z_t. This method is based on the analytic results of the previous theories that represent

220    $\tau_{\mathrm{fp}}(z, z_t)$ as a functional of $D_{\perp}(z)$ and the potential of mean force, $\beta U(z)$[12,13]. According to

221   Ref. 9, $D_{\perp}(z)$ can be obtained from

222    $$D_{\perp}(z) = -\frac{e^{\beta U(z)}}{\partial \tau_{\mathrm{fp}}(z, z_t)/\partial z} \int_{z_{\mathrm{refl}}}^{z} dz' \, e^{-\beta U(z')} . \tag{S16}$$

223   Here, thermal energy scaled potential of mean force, $\beta U(z)$, of water molecules can be

224   calculated from the density profile of water molecules, shown in Figure S2a, i.e., $\beta U(z) \equiv$

225    $-\log[\rho(z)/\rho_{bulk}^{45°C}]$ with $\rho_{bulk}^{45°C}$ being the density of bulk water at 45°C. In eq S16, z_{refl}

226   designates the position of the reflecting boundary. As the number of water molecules passing

227   through the lipid bilayer membrane is negligibly small throughout our MD simulation, we set

228   the reflecting boundary at the membrane center, i.e., $z_{refl} = 0$.

229   To calculate $D_\perp(z)$ using eq S16, we computed the z-dependent profile of $\tau_{fp}(z, z_t)$

230   using our MD trajectories, systematically changing the value of z_t by 1 Å. The various

231   positions of z_t for each system are represented by the dots of different colors in Figure S2a.

232   The z-dependent profiles of MFPT for various values of z_t have the same slope through the

233   entire z range, as shown in Figure S2c. Each solid line in Figure S2c represents $\tau_{fp}(z, z_t)$ with

234   the target position, z_t, represented by the dot of the same color in Figure S2a. As $\partial_z \tau_{fp}(z, z_t)$

235   is independent of z_t, so is $D_\perp(z)$ calculated from eq S15 (see Figure S2d). The profile of

236    $D_\perp(z)$ was well fitted to a multi-Gaussian function,

237
$$D_\perp(z) = y_0 + \sum_{i=1}^{n} \frac{a_i}{\omega_i \sqrt{\pi/2}} \exp\left(-2\left(\frac{z - z_{c,i}}{\omega_i}\right)^2\right),$$
(S17)

238   shown as dotted lines in Figure S2d. The optimized parameters for these fittings are provided

239   in Table S2. These best-fitted results, shown as dotted lines in Figure S2d, are represented by

240   the solid lines in Figure 3d of the main text.

241

242 # Figure S3: Diffusion Kernel Correlation and Non-Gaussian Parameter

(a)

(b)
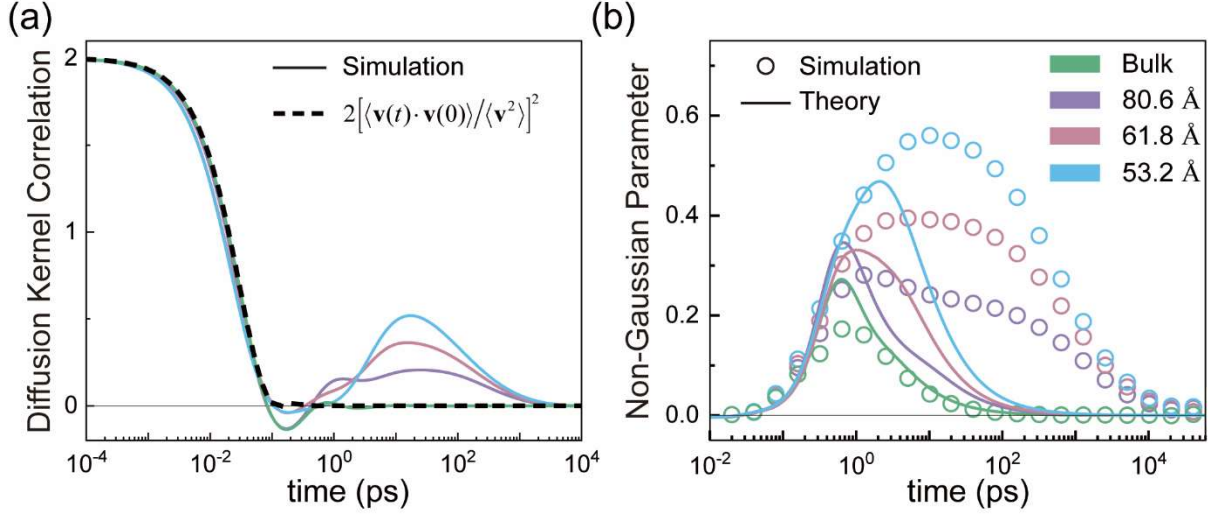
243

244   The lateral diffusion kernel correlation (DKC), $C_{\mathcal{D}}(t)$, is a key dynamic quantity that

245 characterizes the environment-coupled fluctuation of water molecule's motility in the lateral

246 direction. Based on the eq S8, we express the DKC in the Laplace domain as

$$\hat{C}_{\mathcal{D}}(s) = \frac{\hat{\Delta}_4(s)}{4s^2 \hat{\Delta}_2(s)^2} - \frac{1}{s} \tag{S18}$$

247

248 To extract the time-profile of the DKC of water molecules by performing numerical inverse

249 Laplace transform of eq S18, it is convenient to have analytic expressions of the first two non-

250 vanishing moments, $\Delta_2(t)$ and $\Delta_4(t)$, of the distribution of the lateral displacement of water

251 molecules.

252   The time profile of the MSD, $\Delta_2(t)$, is well represented by the following formula

253 according to Ref.14:

$$\Delta_2(t) = 4\frac{k_B T}{M\gamma_0^2} c_0 \left(\gamma_0 t - 1 + e^{-\gamma_0 t}\right) + 4\frac{k_B T}{M} \sum_{i=1}^{2} \frac{c_i}{\omega_{0,i}^2}\left[1 - e^{-\gamma_i t}\left(\cosh\omega_i t + \frac{\gamma_i}{\omega_i}\sinh\omega_i t\right)\right] \tag{S19}$$

254

255 This formula represents the MSD of a bead in a Gaussian polymer composed of three beads in

256 a high friction regime. The first and second terms on the R.H.S of eq 19 account for the

257 contribution from the unbound mode and bound modes, respectively. c_i designates the weight

258 coefficient of ith mode, which satisfies the following condition $\sum_{j=0}^{2} c_j = 1$. The optimized

259 parameters for this fitting are provided in Table S3.

260 The analytic expression of the fourth moment, $\Delta_4(t)$, is obtained from

$$\Delta_4(t) = 2\Delta_2(t)^2[1+\alpha_2(t)] \tag{S20}$$

262 which is obtained from the definition of the NGP. The simulation result for the time profile of

263 the NGP, or $\alpha_2(t)$, could be well fitted to the following function (see Figure 2):

$$\alpha_2(t) \cong \sum_{i=1}^{2\,\text{or}\,3} a_i \exp\left[-\left(\log_{10} t - b_i\right)^2 / c_i\right]. \tag{S21}$$

265 The optimized parameters for this fitting are provided in Table S4. Substituting eqs S19 and

266 S21 into eq S20, we obtain the fully analytic expression of the fourth moment.

267 Taking the Laplace transforms of $\Delta_2(t)$ and $\Delta_4(t)$, and substituting the results into eq

268 S18, we obtain the expression of DKC in the Laplace domain. To obtain the value of DKC at a

269 specific timepoint, t, we perform the numerical Laplace inversion of eq S18, by using the

270 Stehfest algorithm. These results are shown in Figure S3 and Figure 4a. The DKC values in

271 various conditions are shown as solid lines in Figure S3a. At short times, where MSD is not

272 linear in time yet, the DKC can be approximated by $C_{\mathcal{D}}^{(short)}(t) = 2\left[\langle \mathbf{v}(t)\cdot\mathbf{v}(0)\rangle / \langle \mathbf{v}^2\rangle\right]^2 = 2\phi_{\mathbf{v}}^2(t)$

273 [14]. Here, $\mathbf{v}$ denotes the water molecule's velocity vector in the lateral direction, and the

274 velocity autocorrelation function, $\langle \mathbf{v}(t)\cdot\mathbf{v}(0)\rangle$, is equivalent to twice the lateral diffusion

275 kernel, $\langle \mathcal{D}_{\parallel}(t)\rangle$ [14]. From eqs S6 and S19, an analytic expression of the lateral diffusion kernel

276 can be obtained as

$$\frac{\langle \mathcal{D}_\parallel(t) \rangle}{\langle \mathcal{D}_\parallel(0) \rangle} \left(= \frac{\langle \mathbf{v}(t) \cdot \mathbf{v}(0) \rangle}{\langle |\mathbf{v}|^2 \rangle} \right) = c_0 e^{-\gamma_0 t} + \sum_{i=1}^{2} c_i e^{-\gamma_i t} \left[\cosh \omega_i t + \frac{\gamma_i}{\omega_i} \sinh \omega_i t \right] \quad \text{(S22)}$$

278 where $\langle \mathcal{D}_\parallel(0) \rangle$ denotes $k_B T / M$.

279 To verify the correctness of $C_\mathcal{D}(t) \cong 2\phi_\mathbf{v}^2(t)$, we made a comparison between $2\phi_\mathbf{v}^2(t)$ of

280 bulk water, depicted as the dashed line in Figure S3, and the time profile of the DKCs. The

281 agreement between $2\phi_\mathbf{v}^2(t)$ and the DKCs at short times confirms the validity of our short-

282 time asymptotic expression of the DKC. As shown in Figure S3a, the short-time dynamics of

283 the DKC is largely independent of the degree of confinement, or ℓ.

284 The short-time asymptotic expression of the DKC enables us to obtain the short-time

285 asymptotic behavior of $\alpha_2(t) \propto t^2$. Using the asymptotic expression of the DKC in the exact

286 analytic expression of the fourth moment, given in eq S8, we obtain

$$\hat{\Delta}_4(s) \cong 4s\hat{\Delta}_2(s)^2 [1 + s\,\hat{C}_\mathcal{D}^{(short)}(s)]. \quad \text{(S23)}$$

288 Substituting the time-domain version of eq S23 into the definition of the NGP, $\alpha_2(t)$

289 $\left[\equiv \Delta_4(t) / (2\Delta_2(t)^2) - 1 \right]$, we obtain the following short-time asymptotic expression of $\alpha_2(t)$:

$$\alpha_2(t) = \frac{1}{18}\left(\gamma^2 - \mu\right)t^2 + \mathcal{O}(t^3) \quad \text{(S24)}$$

291 In eq S24, γ and μ are given by $\gamma = -\lim_{t \to 0} \partial \phi_\mathbf{v}(t) / \partial t = c_0 \gamma_0 + 2\sum_{i=1}^{n} c_i \gamma_i$ and

292 $\mu = \lim_{t \to 0} \partial^2 \phi_\mathbf{v}(t) / \partial t^2 = c_0 \gamma_0^2 + \sum_{i=1}^{n} c_i \left(3\gamma_i^2 + \omega_i^2\right)$, respectively[14]. These results are shown as

293 the solid lines in Figure S3b. The short-time asymptotic behavior of the NGP given in eq S24

294 is found to be in good quantitative agreement with our MD simulations results.

295   # Figure S4: Relationship between DKC and NGP at long times
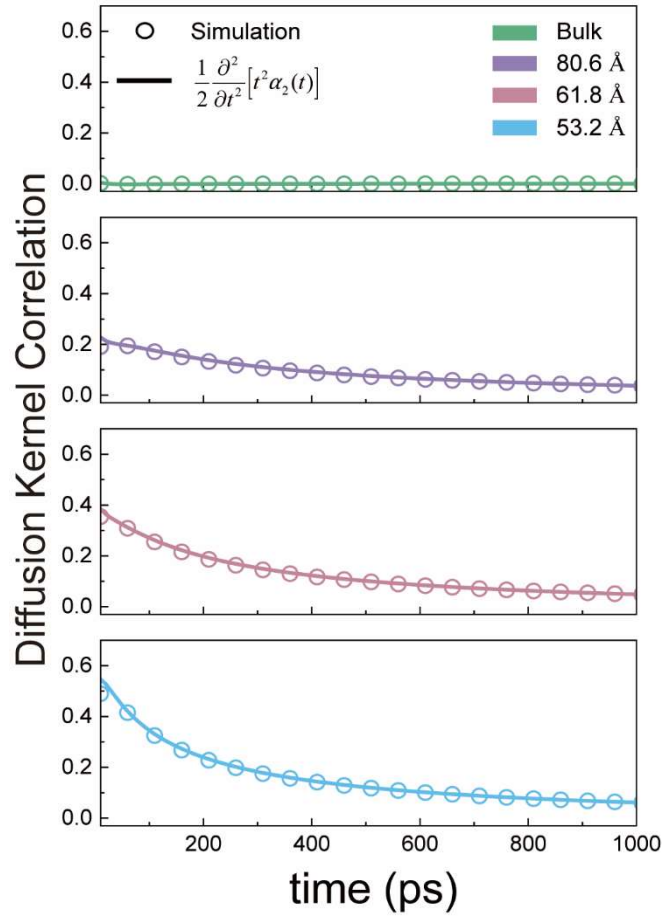
296

297   The relaxation dynamics of the DKC, $C_{\mathcal{D}}(t)$, determines the NGP time profile of water

298   molecules in the intermembrane space after the onset of Fickian diffusion, where the time

299   profile of $C_{\mathcal{D}}(t)$ can be obtained by the NGP time profile, i.e.,

300
$$C_{\mathcal{D}}(t) \cong \eta_D^2 \phi_D(t) = \frac{1}{2}\frac{\partial^2}{\partial t^2}[t^2 \alpha_2(t)]. \tag{S25}$$

301   Solid lines in Figure S4 represent the time profiles of $C_{\mathcal{D}}(t)$ obtained from eqs S25 and S21.

302   Circles represent the time profiles of $C_{\mathcal{D}}(t)$ extracted from our MD simulation results, using

303   the method described in the paragraph below Figure S3.

304

Caption for Movie S1: Heatmap of discrete Green's function

As we mentioned in the main text, linear dependence between τ_D and ℓ^2, as shown in the inset of Figure 4a, arises because the time taken for water molecules to traverse the entire intermembrane space increases quadratically with separation, ℓ, between center membranes. To show the stochastic transport dynamics of water molecules at various initial positions, we present a movie showing the time-dependent changes in the probability distribution of water molecules in the intermembrane space. For this purpose, we first discretize the intermembrane space into three regions: two interfacial regions near the two membranes confining the water molecules, defined by $z < z_c$ and $z > \ell - z_c$ with $z_c = 23.6$ Å, and one bulk water-like region between the two interfacial regions (see Figure 3 in the main text). The bulk water-like region does not exist for our system with $\ell = 53.2$ Å; however, it exists for our system with a greater value of intermembrane separation ℓ.

We identify the entire bulk water-like region as a single layer named layer 0. Each interfacial water region is divided into 5 layers. Specifically, the interfacial water region on the left side is divided into the following layers: (i) 0 Å $\leq z < 15.2$ Å, (ii) 15.2 $\leq z <$ 18 Å, (iii) 18 Å $\leq z <$ 20.8 Å, (iv) 20.8 Å $\leq z <$ 23.6 Å, and (v) 23.6 Å $\leq z < z_c$ ($= 26.6$ Å). These layers are respectively labeled as -5, -4, -3, -2, and -1 layers. Similarly, the interfacial water region on the right side is divided from the membrane center on the right side with identical widths, and the corresponding layers are designated as 5, 4, 3, 2, 1 layer, respectively. Consequently, the total number of layers is 11 for $\ell = 80.6$ Å and $\ell = 61.8$ Å, and 10 for $\ell = 53.2$ Å.

326   In Supplemental Movie, we show how the spatial distribution of water molecules in each

327   layer changes over time. For this purpose, we present heat maps, each of which represents the

328   probability distribution of water molecules for our system at a given time. In each heat map,

329   the color of the cell in the n-th column and m-th row represents the probability, $g(n,t|m)$, that

330   a water molecule initially located in the m-th layer is found in the n-th layer at time t. By

331   definition, the initial condition of $g(n,t|m)$ is given by $\lim_{t \to 0} g(n,t|m) = \delta_{nm}$ where δ_{nm}

332   designates Kronecker's delta.

333   The evolving heatmap patterns, as shown in Supplemental Movie, clearly demonstrate

334   that the time required to reach the equilibrium state increases with the length of ℓ. Specifically,

335   in the system with $\ell = 80.6$ Å, water molecules located in the interfacial region do not

336   transfer to the opposite side of the interfacial water region within the first 50 ps. This behavior

337   can be attributed to the increased size of the bulk-water-like region, which hinders the fast

338   exchange of water molecules between the interfacial water regions.

Tables S1-S4

ℓ (Å)	80.6	61.8	53.2
y_0	0.007	0.008	0.005
a_1	0.636	0.374	0.029
a_2	0.636	0.374	0.029
a_3	5.061	4.412	1.951
a_4	5.061		
a_5	0.721		
ω_1	5.944	4.797	4.079
ω_2	5.944	4.797	4.079
ω_3	12.226	11.100	7.449
ω_4	12.226		
ω_5	7.060		
$z_{c,1}$	-14.750	-6.131	-10.790
$z_{c,2}$	14.750	6.131	10.790
$z_{c,3}$	-8.002	0	0
$z_{c,4}$	8.002		
$z_{c,5}$	0		

Table S1. Lateral diffusion coefficient fitting parameters (eq S14).

ℓ (Å)	80.6	61.8	53.2
y_0	0.021	0.018	0.014
a_1	0.063	-0.400	0.973
a_2	0.058	-0.400	0.953
a_3	3.122	5.460	0.055
a_4	2.286		
a_5	1.015		
a_6	0.974		
a_7	2.138		
a_8	1.826		
ω_1	5.873	6.282	5.554
ω_2	5.856	6.281	16.780
ω_3	8.568	12.991	1.901
ω_4	8.089		
ω_5	5.958		
ω_6	6.136		
ω_7	7.413		
ω_8	13.114		
$z_{c,1}$	-22.820	-9.125	0
$z_{c,2}$	22.777	9.125	0
$z_{c,3}$	-11.448	0	0
$z_{c,4}$	11.914		
$z_{c,5}$	-5.603		
$z_{c,6}$	5.456		
$z_{c,7}$	-0.453		
$z_{c,8}$	5.456		

342   **Table S2.** Longitudinal diffusion coefficient fitting parameters (eq S17).

343

	Bulk	$\ell = 80.6$ Å	$\ell = 61.8$ Å	$\ell = 53.2$ Å
c_0	0.0552	0.0624	0.0126	0.0970
c_1	0.0386	0.0403	0.4937	0.4515
c_2	0.9062	0.8973	0.4937	0.4515
γ_0	2.0867	3.2698	0.9116	11.4206
γ_1	2.1041	4.9715	9.8813	11.4206
γ_2	9.1332	9.5602	11.0886	11.7578
$\omega_{0,1}$	2.1041	1.8450	9.8813	11.4206
$\omega_{0,2}$	9.1332	9.5602	4.4480	6.0659
ω_1	0.0017	4.6165	0.0001	0.0002
ω_2	0.0018	0.0026	10.1574	6.0659

Table S3. Diffusion Kernel fitting parameters (eq S19).

	Bulk	$\ell = 80.6$ Å	$\ell = 61.8$ Å	$\ell = 53.2$ Å
a_1	0.166	0.247	0.269	0.263
a_2	0.021	0.105	0.131	0.513
a_3		0.191	0.330	
b_1	-0.111	0.007	0.018	0.210
b_2	0.961	1.041	0.916	1.633
b_3		2.148	1.925	
c_1	0.606	0.637	0.618	0.817
c_2	0.713	0.584	0.607	2.279
c_3		1.634	1.864	

Table S4. NGP fitting parameters (eq S21).

Supplementary References

(1)   Lee, J.; Cheng, X.; Swails, J. M.; Yeom, M. S.; Eastman, P. K.; Lemkul, J. A.; Wei, S.;
        Buckner, J.; Jeong, J. C.; Qi, Y.; Jo, S.; Pande, V. S.; Case, D. A.; Brooks, C. L.;
        MacKerell, A. D.; Klauda, J. B.; Im, W. CHARMM-GUI Input Generator for NAMD,
        GROMACS, AMBER, OpenMM, and CHARMM/OpenMM Simulations Using the
        CHARMM36 Additive Force Field. *J. Chem. Theory Comput.* **2016**, *12* (1), 405–413.

(2)   Lee, J.; Hitzenberger, M.; Rieger, M.; Kern, N. R.; Zacharias, M.; Im, W. CHARMM-
        GUI Supports the Amber Force Fields. *J. Chem. Phys.* **2020**, *153* (3), 035103.

(3)   Wu, E. L.; Cheng, X.; Jo, S.; Rui, H.; Song, K. C.; Dávila-Contreras, E. M.; Qi, Y.; Lee,
        J.; Monje-Galvan, V.; Venable, R. M.; Klauda, J. B.; Im, W. CHARMM-GUI *Membrane
        Builder* toward Realistic Biological Membrane Simulations. *J. Comput. Chem.* **2014**, *35*
        (27), 1997–2004.

(4)   Jo, S.; Lim, J. B.; Klauda, J. B.; Im, W. CHARMM-GUI Membrane Builder for Mixed
        Bilayers and Its Application to Yeast Membranes. *Biophys. J.* **2009**, *97* (1), 50–58.

(5)   Jo, S.; Kim, T.; Im, W. Automated Builder and Database of Protein/Membrane
        Complexes for Molecular Dynamics Simulations. *PLoS One* **2007**, *2* (9), e880.

(6)   Jo, S.; Kim, T.; Iyer, V. G.; Im, W. CHARMM-GUI: A Web-based Graphical User
        Interface for CHARMM. *J. Comput. Chem.* **2008**, *29* (11), 1859–1865.

(7)   Dickson, C. J.; Madej, B. D.; Skjevik, Å. A.; Betz, R. M.; Teigen, K.; Gould, I. R.;
        Walker, R. C. Lipid14: The Amber Lipid Force Field. *J. Chem. Theory Comput.* **2014**,
        10 (2), 865–879.

(8)   Darden, T.; York, D.; Pedersen, L. Particle Mesh Ewald: An N·log(N) Method for Ewald

373   Sums in Large Systems. *J. Chem. Phys.* **1993**, *98* (12), 10089–10092.

374   (9)   Hinczewski, M.; Von Hansen, Y.; Dzubiella, J.; Netz, R. R. How the Diffusivity Profile

375   Reduces the Arbitrariness of Protein Folding Free Energies. *J. Chem. Phys.* **2010**, *132*

376   (24), 245103.

377   (10)   Sedlmeier, F.; von Hansen, Y.; Mengyu, L.; Horinek, D.; Netz, R. R. Water Dynamics at

378   Interfaces and Solutes: Disentangling Free Energy and Diffusivity Contributions. *J. Stat.*

379   *Phys.* **2011**, *145* (2), 240–252.

380   (11)   von Hansen, Y.; Gekle, S.; Netz, R. R. Anomalous Anisotropic Diffusion Dynamics of

381   Hydration Water at Lipid Membranes. *Phys. Rev. Lett.* **2013**, *111* (11), 118103.

382   (12)   Weiss, G. H. First Passage Time Problems in Chemical Physics. In *Advances in*

383   *Chemical Physics*; I. Prigogine (Ed.), 1967; pp 1–18.

384   (13)   Szabo, A.; Schulten, K.; Schulten, Z. First Passage Time Approach to Diffusion

385   Controlled Reactions. *J. Chem. Phys.* **1980**, *72* (8), 4350–4357.

386   (14)   Song, S.; Park, S. J.; Kim, M.; Kim, J. S.; Sung, B. J.; Lee, S.; Kim, J.-H.; Sung, J.

387   Transport Dynamics of Complex Fluids. *Proc. Natl. Acad. Sci. U.S.A.* **2019**, *116* (26),

388   12733–12742.

389